Supplementary Material

for "The alignment of vortical structures in turbulent flow through a contraction"

by Mugundhan, Pugazenthi, Speirs, Samtaney & Thoroddsen

S1. Photographs of the Experimental Setup

(a) (b)

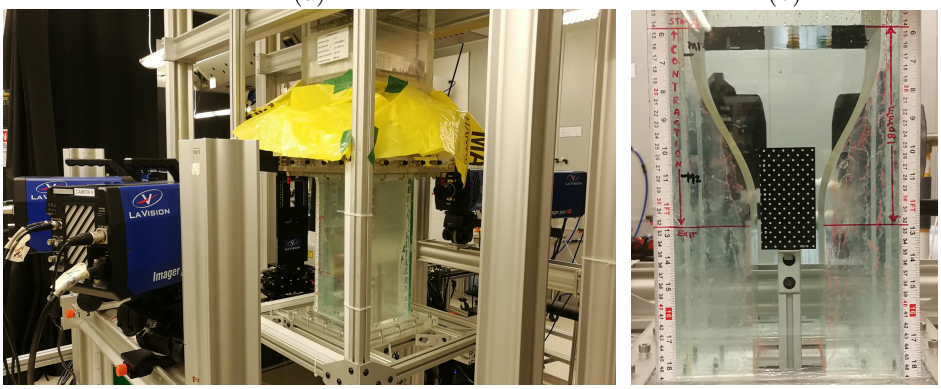

Figure S1: (a) Closer view of the glass-acrylic contraction with the active grid covered with water-proof yellow sheets. (b) The contraction with calibration plate mounted in measurement region P3. The calibration plate is supported using an aluminum support-strut extending from the bottom of the tunnel. The water level used during calibration, is visible at the inlet of the contraction.

(a) (b)

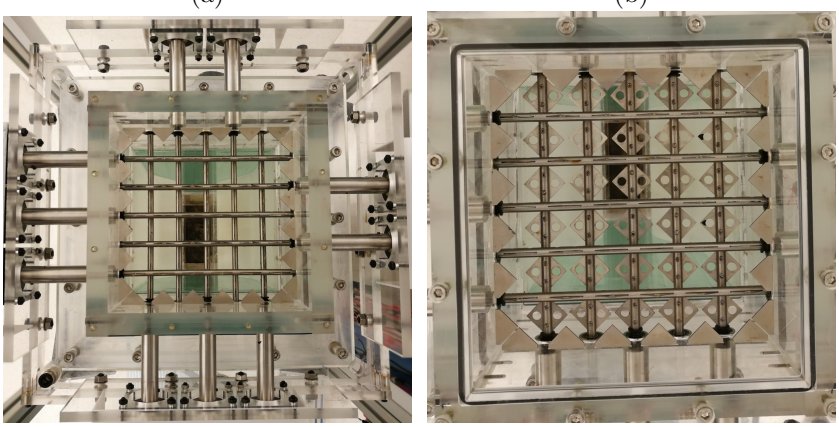

Figure S2: A top view of the active grid with all flaps open is shown in (a) and only the top flaps open in (b). The view is from the top, down towards the contraction, without the inlet section in place. The rotation cycle starts from the position shown in (b) condition in modes S2 and S4.

S2. Tomo-PIV and STB Calculations

We carried out a systematic study to determine the best spatial resolution to use for the velocity calculations by Tomographic PIV direct correlation (referred as just Tomo) and Shake-The-Box (STB) methods. The typical raw image-quality from the cameras is shown in figure S3. Calculations are for the complete set of images captured for one of the realizations in measurement region P2, with the grid rotating in mode S1. Here, the interrogation resolution in the Tomo calculations corresponds to the correlation volume size and the overlap percentage. In the STB it is the grid to which the Lagrangian velocities are mapped onto. The various resolutions we used for the grid-dependence study are summarized in Table. S1. For the Tomo calculations, direct correlation with binning is used. We use multi-step correlation windows with progressively decreasing window sizes starting from 128, where two passes in each size are employed. The size specified in Table. S1 is the finest size used in the multi-step technique. In the STB calculations, a cubic polynomial is used for particle-track conversion with 5 and 11 time-step filter lengths. We use an overlap of 75% in all cases for high spatial resolution, even though adjacent vectors are not fully independent. The effect of overlap percentage on the results has not been considered.

Schanz *et al.* (2016) describe the steps involved in the STB calculations. They classify the steps involved into three phases: (1) Initialization, (2) Convergence and (3) Converged phase. To start with, there are no tracks for applying the algorithm to. These tracks are obtained in the first phase. Particle candidates are identified by triangulation for the first few time steps (usually 4 time steps) and with the obtained 3D distribution, trajectories are extracted using matching between subsequent frames. Following this, in the convergence phase, particles tracked for the previous t^k time steps are used with Wiener filter, to extrapolate their position to the next time level t^{k+1}. The actual positions of the predicted particles are obtained by minimizing the residual images by a 'shaking' procedure implemented in Iterative Reconstruction of Volume Particle Distribution (IPR) (Weineke (2013)). The position and intensity of the predicted particles are then corrected. Having obtained the correct positions, new particles entering the measurement zone (those with no previous track history) are added to track list and, while those leaving are removed from the list. In the final converged phase, the number of tracks gets stabilized around a constant value, with number of particles entering the measurement volume becoming approximately equal to those leaving. Having obtained the track history of particles, a third order B-spline is fit for the time series of corresponding coordinates with an appropriate time filter length. First and second derivative of the spline give the velocity and acceleration respectively.

An iterative technique called "FlowFit" (Gesemann (2015)) is employed for interpolations of the available velocity data along the tracks onto a regular Eulerian grid. Additional conditions on the curvatures of the splines and divergence of velocity in each cell are imposed during the conversion to the Eulerian grid. Schanz *et al.* (2016) evaluated their STB algorithm systematically using a set of synthetic particle images with different seeding densities and noise. They show STB results with very low ghost particles (< 0.04 %) and high accuracy in position (average error 0.018 pixels) even at very high concentration of 0.125 ppp. They also compare STB with Tomo-PIV (with the SMART algorithm for reconstruction and 3D direct correlation) by analyzing an experiment on transitional jet. STB results in very good temporal coherence of structures. They estimate the computational time required for STB to be 7.5 times less than the time required for Tomo-PIV.

Figure S4 shows the instantaneous z-vorticity distribution obtained for the different

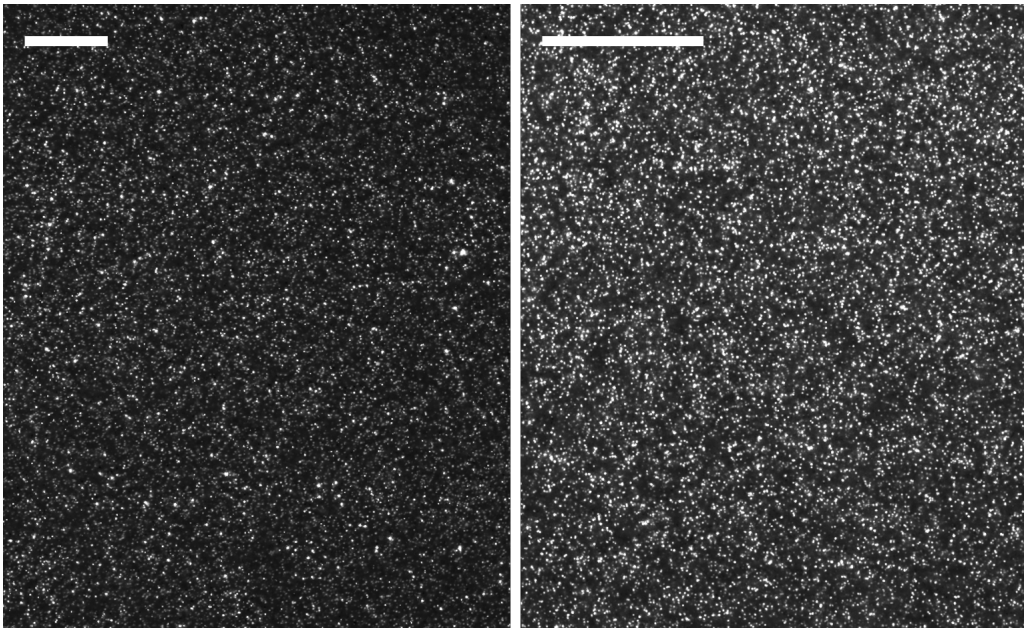

Figure S3: Sections of typical raw particle images obtained in experiments with the normal magnification (left) and high-magnification (right). The scale bars in the figures represent 5 mm. The pixel areas shown are 750×930 px. Particle concentration is $\sim$ 0.03-0.04 particles-per-pixel (ppp).

resolutions. Comparing Tomo and STB, we see both methods capturing the big-scale vortical structures, across all grid sizes. However, there is a significant difference in shapes of the smaller structures. With smaller grids we observe finer structures to be better resolved, but it is essential to determine if they are physical and do not arise from noise. The lower limit on the grid is decided based on the traceability of structures with time. It is seen that with 32 and 28 voxels, these structures are not easily traceable in time, with changes in the vorticity field becoming abrupt. Thus these finest resolutions are not used herein. On the other hand, with too coarse a grid, it is possible to trace structures very distinctly with time, but true fine-scale fluctuations may get smoothed out. Thus it is essential we arrive at the appropriate grid size. We use RMS statistics of the velocity and vorticity fields, along the centerline of the tunnel, to help guide this choice.

In Tomo-PIV the primary control parameter is the size of the interrogation volume, while in STB the time-tracking adds a new dimension where smoothing in time enters as an additional parameter. Figure S5 shows the effect of time-filter length for the STB calculations for two resolutions, i.e. 48 and 36 voxels. Mean velocity (figure S5(a)) is independent of both grid size and time-filter length, with indistinguishable curves. Despite the greater smoothing from using longer time-filter length, this only very slightly under-predicts the fluctuations, as is seen in the RMS streamwise velocity (figure S5(b)) and RMS spanwise vorticity (figure S5(c)). The spatial resolution has much stronger effect on the RMS magnitudes, with the 36-voxels velocity results as much as 8% higher than for the 48-voxels. The fluctuating vorticity is more sensitive to the length-scale, giving up to 40% higher RMS using the finer resolution.

We next compare the results of Tomo and STB results for different grid sizes in figure S6. Tomo is calculated at 48, 40 and 32 voxels and compared to STB at 48, 36 and 32 voxels. Even though it was shown above that the 32-voxels results give noisy results,

Method	Correlation Size - Overlap (voxels)	Resolution (voxels)	Resolution (mm)
Tomo	48 - 75%	12	0.62
Tomo	40 - 75%	10	0.52
Tomo	32 - 75%	8	0.41
Tomo	28 - 75%	7	0.36
STB	48×48×48 - 75%	12	0.62
STB	36×36×36 - 75%	9	0.46
STB	32×32×32 - 75%	8	0.41
STB	28×28×28 - 75%	7	0.36

Table S1: Parameters used for Tomographic and STB calculations.

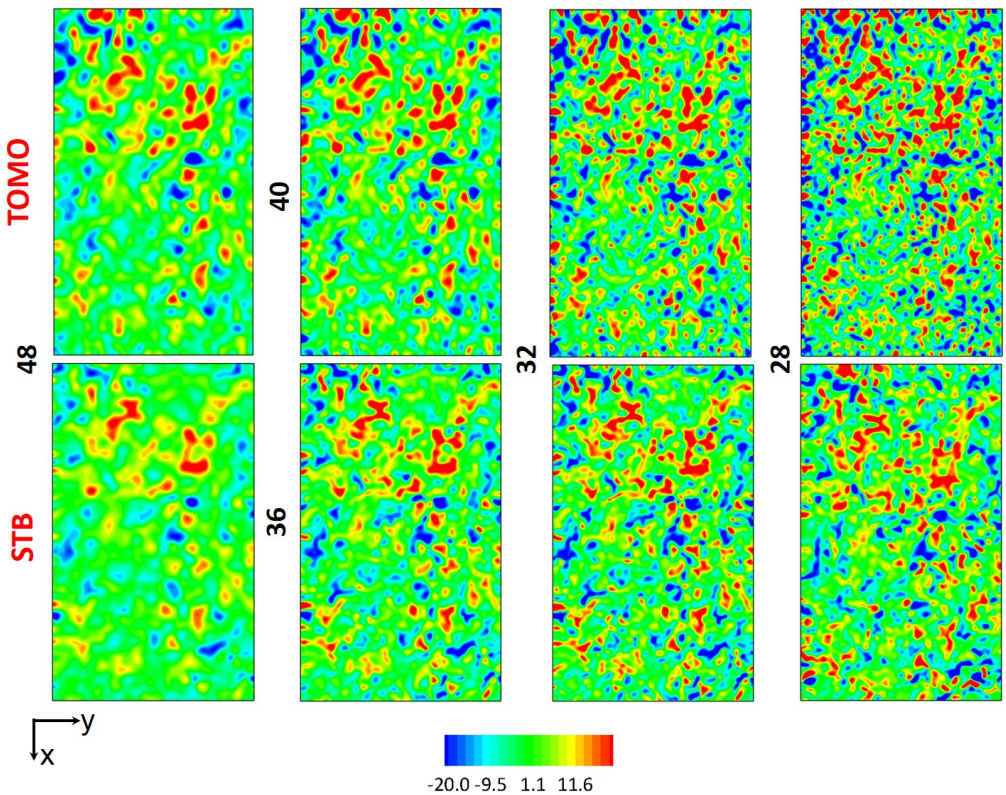

Figure S4: Comparison of instantaneous contours of ω_z for different spatial grid sizes, from Tomo and STB calculations. The areas are 56×106 mm.

(a)

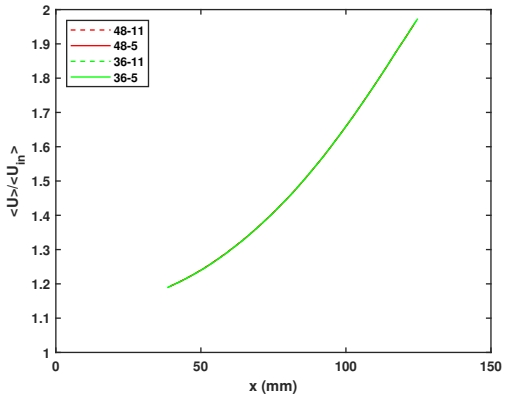

(b)

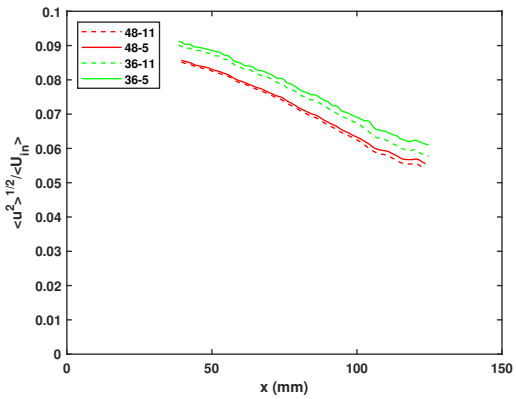

(c)

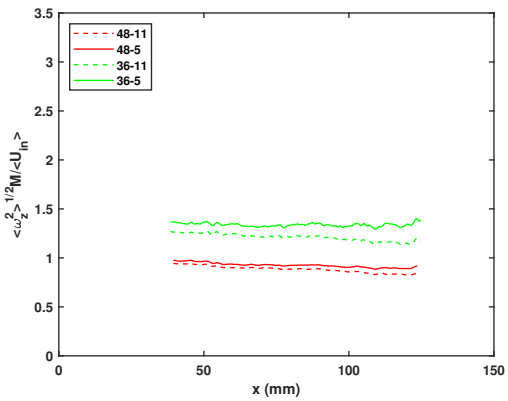

Figure S5: Effect of time-filter length on the STB calculations inside the contraction in region P2. (a) Mean streamwise velocity $\langle U \rangle$. The curves are all indistinguishable. (b) u_{rms}, (c) $\omega_{z,rms}$. Results are shown for two grids, 48×48×48 and 36×36×36 voxels and two time-filter lengths of 11 and 5 time steps.

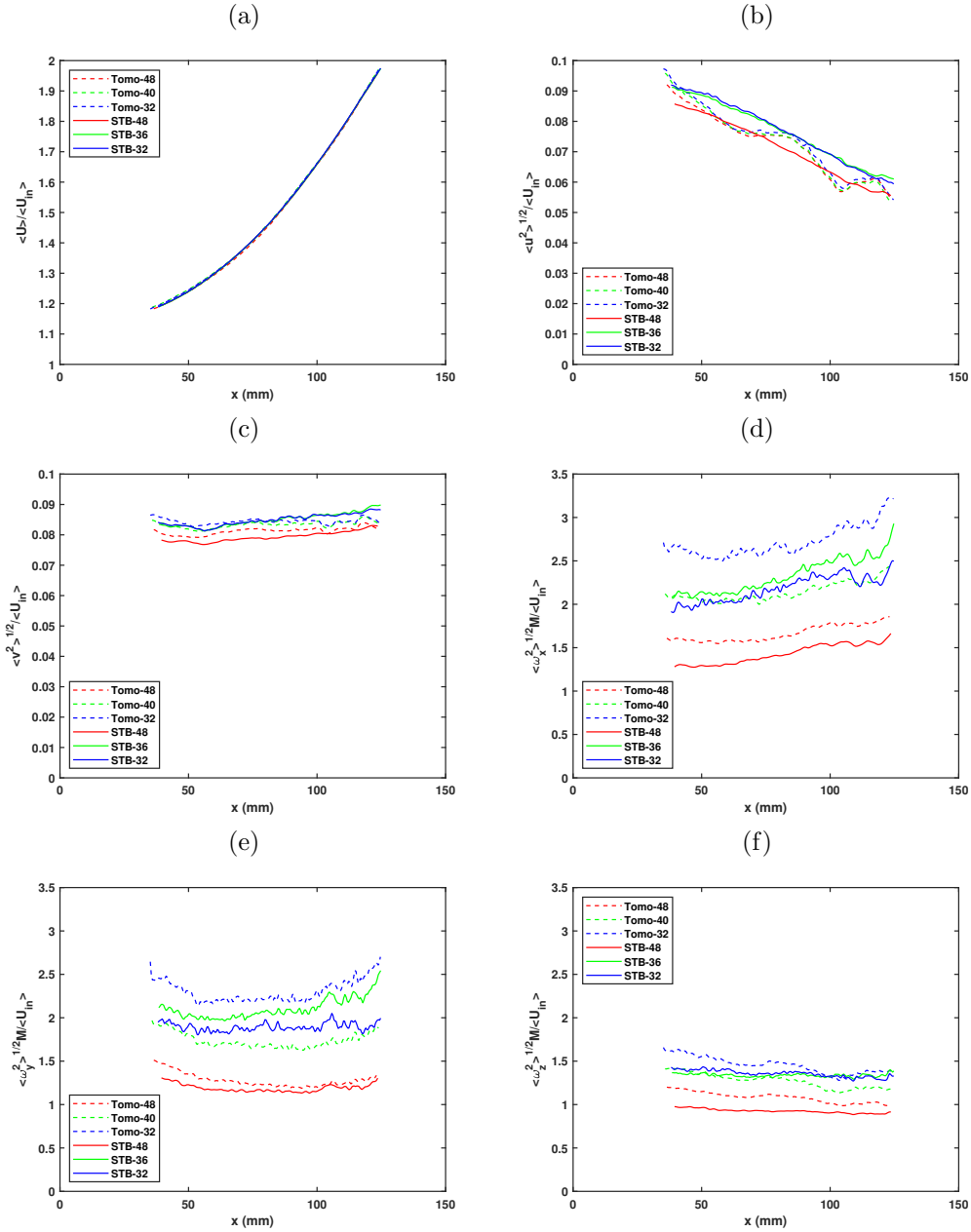

Figure S6: Comparison of Tomo and STB calculations for different grids. (a) Mean stream wise velocity $\langle U \rangle$, (b) u_{rms}, (c) v_{rms}, (d) $\omega_{x,rms}$, (e) $\omega_{y,rms}$, (f) $\omega_{z,rms}$. The STB results presented are all with 5 time-step filter length.

we include them in the below statistics for comparison. The mean streamwise-velocity results are independent of the method and the grid-resolution used, with all the curves in figure S6(a) being identical. The RMS velocity predictions by Tomo and STB look fairly similar (Fig S6 (b) and (c)). On the other hand the STB results for the largest grid are suppressed by 5% compared to the similar results for 36 and 32 voxels.

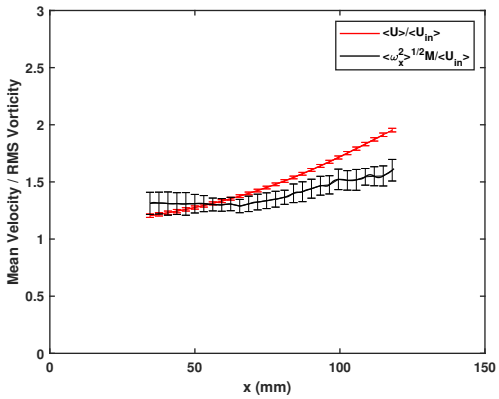

Figure S7: Mean velocity and RMS vorticity with error bars, in position P2, for grid-rotation Mode S1. Error bars correspond to the RMS variation between the four experimental runs. For clarity, bands have been shown for every fifth point in x.

Looking at the vorticity (figure S6 (d), (e) and (f)), Tomo predictions are consistently higher than those of STB. In general, we see a large increase in the vorticity fluctuations with smaller grids, which arises from the spatial derivative in its definition.

From these and similar results we conclude grids with 36 voxels, can overpredict the RMS and henceforth use 48 voxel grids for the RMS statistics and coherent structure identification, while retaining 36 voxels for the PDFs.

S3. Error quantification

Figure S7 shows the typical measurements error bars associated with the statistical estimates, for both the mean velocity data and RMS vorticity data. The error computations are made using the four independent realizations for the base grid-rotation mode S1, inside the contraction in position P2. Error bands shown in the figure correspond to the RMS of the measurements.

The average values for RMS as a percentage of the corresponding mean values are:
(1) Mean velocity $\langle U \rangle$ is 0.9%;
(2) RMS velocities u_{rms}, v_{rms}, w_{rms} are 3.5%, 4.3%, and 5.5%; and
(3) RMS vorticity $\omega_{x,rms}$, $\omega_{y,rms}$, $\omega_{z,rms}$ are 5.7%, 5.1%, and 6.0% respectively.

It is clear from these results that the $w-$component, i.e. in the direction most perpendicular to the four cameras, has the largest noise. This is the velocity component across the span of the laser volume, which is consistent with errors in Stereo-PIV.

S4. Convergence

In order to verify the convergence and repeatability of our results we perform another set of experiments at position P3 for grid-rotation mode S1. In figure S8 we show the streamwise evolution of RMS velocities for different realizations, which were taken on the same day under similar conditions. Keep in mind that the tunnel must be turned off between every run, while the data is downloaded from the cameras to the computer. Runs must therefore be spaced by about one hour. These runs all show similar trends with acceptable variation. The average values for RMS as a percentage of their corresponding

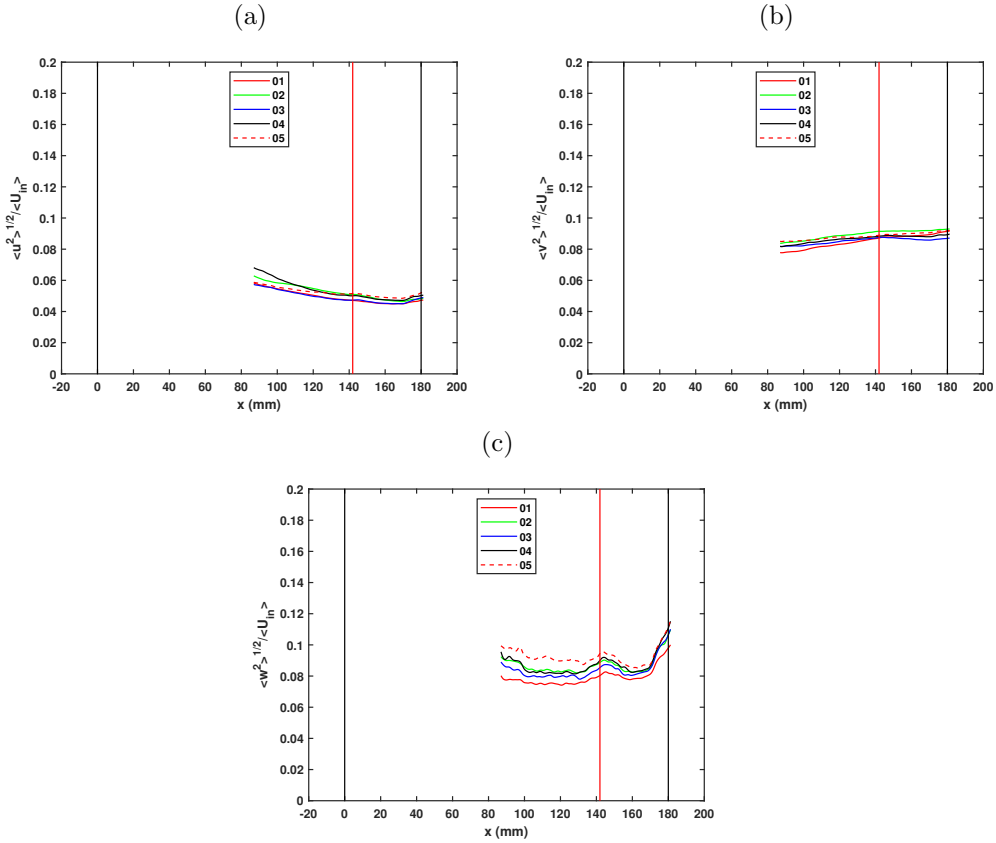

Figure S8: Convergence of streamwise statistics at position P3 for grid-rotation mode S1. Comparison of statistics obtained from different realizations made on the same day. The quantities shown are: (a) u_{rms}, (b) v_{rms}, (c) w_{rms}. Vertical black lines represent the start and end of contraction and the vertical red line marks MCL. Numbers in the legend correspond to the different realization.

mean values of u_{rms}, v_{rms}, w_{rms} are 2.3%, 3.9% and 5.3%. We notice that the depth-wise component w_{rms} has the maximum deviation as expected from our camera alignments and the Tomographic algorithms. However, we still notice the local peak in w_{rms} in all the realization which is consistent with our earlier measurements, in figure 9(c).

S5. Effect of grid-rotation modes on homogeneity of the flow

Figure S9 shows the transverse contours of the mean streamwise velocity component ($\langle U \rangle / \langle U_{in} \rangle$) at different locations x= −110, −90, −70, −50 and −30 mm, for the four different synchronous modes. These locations are close to the active grid and all are chosen to be upstream of the start of the contraction, The mean flow in the experiments is in the x direction. The signature of the grid location and rotation on the mean flow is imprinted on these contours. To illustrate this, a schematic of the measurement region P1 with respect to the active grid is shown in figure S10. It also shows the simplified velocity profile of flap-induced fluctuation for grid-rotation modes S1 and S2. The measurement region lies in the downstream rectangular prism included vertically between bottom shafts M7, M6 and top shafts M4, M5. Figure S10 shows the top view of the measurement region

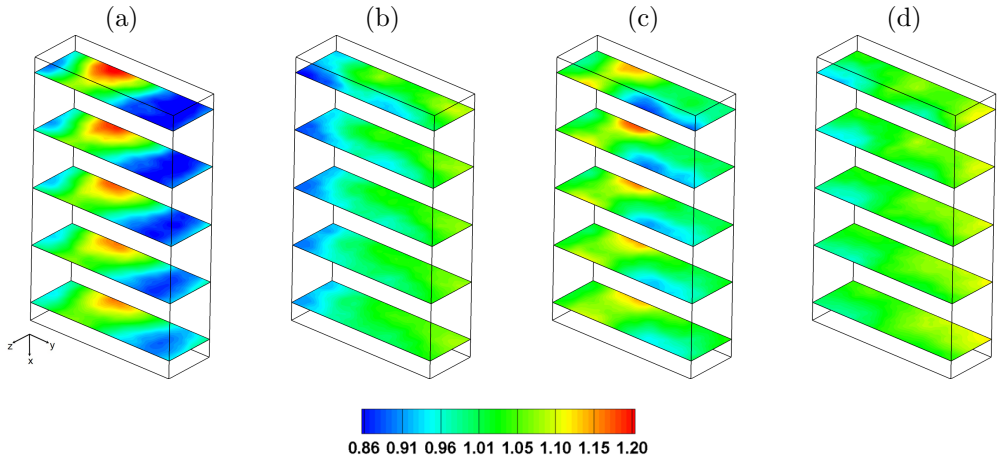

Figure S9: Transverse contours of the time-averaged streamwise velocity ($\langle U \rangle / \langle U_{in} \rangle$) for modes (a) S1, (b) S2, (c) S3, and (d) S4, at streamwise cross-sections, $x = -110$, -90, -70, -50 and -30 mm ($x_{AG}/M \approx 4.3$, 5, 5.6, 6.3 and 7) within the volumetric measurement region P1. The mean flow is in the positive x direction. Dimensions of the cross-sections shown are 55.9 mm $\times$ 19.0 mm. The coordinate symbol in (a) indicates the principal directions and does not coincide with the actual origin.

in dotted lines relative to projections of these six shafts and their flaps (only flaps directly above the measurement region are shown). Four quadrants formed by these six shafts are numbered I, II, III, IV in anti-clockwise direction starting from top right.

The simplest possible model adds the local normal velocity of the flap to the mean flow. The local normal velocity of a flap is a linear function of its radial distance from the shaft axis, and thus the velocity fluctuations induced on the mean flow is also assumed to be a linear function. Figure S10(b) shows the profiles of flap induced fluctuations for the region for modes S1 and S2. For simplicity, separation distance between the shaft planes and flap holes have not been considered. These factors have significant effect on the flow locally, and the actual flow is much more complex than the representation here with the vorticity induced by flow separation from the tips of the blades. However, this simplified model helps to qualitatively verify the velocity distribution obtained from the current analysis. As seen in figure S10(a), the measurement region does not occupy all of the four quadrants. Figure S10(c) shows a closer view of the measurement region with the projected flap positions, and the direction of velocity induced by the flaps.

In mode S1, shafts M7, M6, M9 rotate clockwise, and M2, M4, M5 rotate anti-clockwise (when viewed in $-y$ and $-z$ directions). Due to this combination, the induced fluctuations have a velocity profile of periodicity $2M$. There is a net downward velocity addition to the mean flow in quadrant II (all flaps in II move down); and a net upward velocity against the downward mean flow in quadrant IV (all flaps in IV move up). This is consistent with the curves shown in figure S11, where we present the phase-averaged streamwise velocity for this mode. Results show phase-averaged velocity at five different points specified in the caption of figure S11. They are shown over half of a revolution of the flaps due to the symmetry of the two blades. In this figure, angle zero corresponds to the start of acquisition of images and not the home position of flaps which were not synchronized with the cameras. This half of a revolution with a period of $T/2 \approx 168$ ms constitutes one cycle. Phase averaging is done by taking the mean of velocities (locally averaged

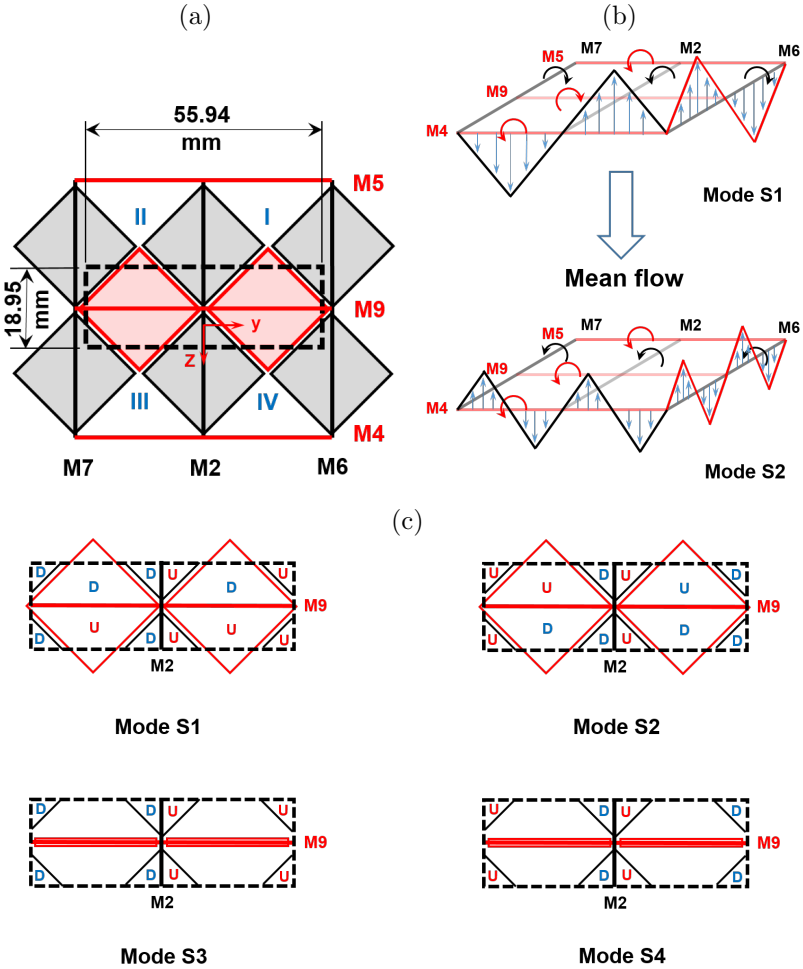

Figure S10: (a) Schematic of the measurement region P1 (dotted lines) relative to the projected view of the shafts and flaps. The y-z view of P1 is viewed from the top in the flow direction. The four quadrants of the flap configuration are marked I, II, III and IV. Top plane shafts/flaps shown in red, bottom grid-plane in black. (b) Idealistic velocity profiles of flaps for modes S1 and S2. (c) Closer view of the measurement region relative to the direction of velocity induced by the flaps. U-upward ($-x$); D-downward ($+x$). The thick red lines in S3 and S4 indicate the stationary vertical flaps for those modes.

over 8 time steps) corresponding to approximately the same position of the flaps, over 32 repeating grid-oscillation cycles during one complete time-series. Point QII which sits below fully downward-moving flaps (refer to figure S10(c)) shows the highest velocity (green curve in figure S11). Its velocity profile shows twice the periodicity of the flap, which is due to interaction of adjacent flaps motion. Point QIV which is downstream of all upward moving flaps, shows the lowest velocity wherein the flaps move against the mean stream (black curve in figure S11). Points QI and QIII (solid red and blue curves) in quadrants I and III, have both upward and downward velocity additions due to opposing flaps. Point CL shows a velocity in between the other locations due to the effects from all the flaps. The velocity magnitudes observed at all these points is in line with the contour

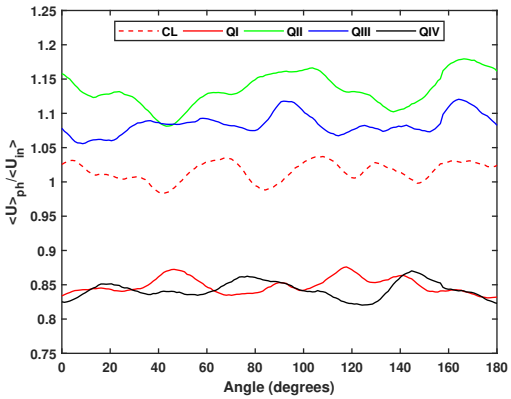

Figure S11: Phase-averaged streamwise velocity for mode S1. The averaging is done over about 32 half-cycles of the flaps. Results are shown at different locations in the horizontal plane $x = -110$ mm. The specific locations are at the CL-centerline and center points of the quadrants I, II, III, IV of the dotted region shown in figure S10(a) which are named QI, QII, QIII, QIV respectively.

plots shown in figure S9(a). Points QII and QIII show higher downward mean velocity, similar to higher magnitude on the left half of the measurement region (when viewed from C1). Due to the varying effects of the flaps and sufficient distance downstream of the grid, different periodicities are exhibited at different locations.

For mode S2, in which adjacent shafts rotate in the same direction, fluctuations have a spatial periodicity M. All four quadrants have both upward and downward velocity additions. Thus, a larger section of the plane has the mean value $\langle U_{in} \rangle$ (figure S9 (b)). Protocols of modes S3, S4 are similar to modes S1 and S2 respectively, except that the top flaps are kept fixed in vertical open position (red flaps are open), and these do not contribute significantly to the turbulence. Modes S3 and S4 show the corresponding behavior together with the effect of upstream static shafts. Due to energy addition only from the bottom shafts, modes S3 and S4 have relatively lower magnitudes as seen in figure S9. At $x = -110$ mm, there is larger non-uniformity with modes S1, S2, whereas with S2, S4 streamwise velocity is more uniform. For all modes the transverse inhomogeneities in mean velocity decrease by the strong turbulent transport as we move downstream. However, with modes S1, S3 flow remains significantly non-uniform even at $x = -30$ mm.

S6. Increase of distance between the grid and contraction

In section 3.9, we describe our experiments with the extensional part, which was added to increase the distance between the grid and the contraction. In these experiments the measurement regions are slightly displaced in the streamwise direction as compared to P2 and P3, without extensional part, but the width and thickness of the illuminated volume remains the same. We call these regions P2* ($x = 3$ mm to 109 mm) and P3* ($x = 86$ mm to 192 mm). P2* is 20 mm above region P2 and is closer to the inlet of the contraction. This repositioning of the measurement region was caused by modification of the calibration plate. However the two combined regions cover the entire length of the contraction.

In terms of distance from the active grid we now have x_{AG}/M varying from 16 to 22.

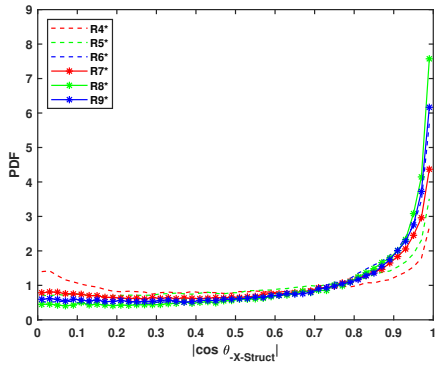

Figure S12: Streamwise evolution of the orientation PDF of coherent vortical structures in sub-regions R4*-R9*. PDFs shown are for mode S1. Structures are identified using the criteria of size > 100 voxels and $|\boldsymbol{\omega}|$= 20 s^{-1} PDFs are evaluated with 50 bins. The mid-x locations (in mm) for the sub-regions are: 20 (R4*), 55 (R5*), 90 (R6*), 103 (R7*), 138 (R8*), 173 (R9*). The peak PDF value increases through the contraction before reducing slightly in the last location below its exit.

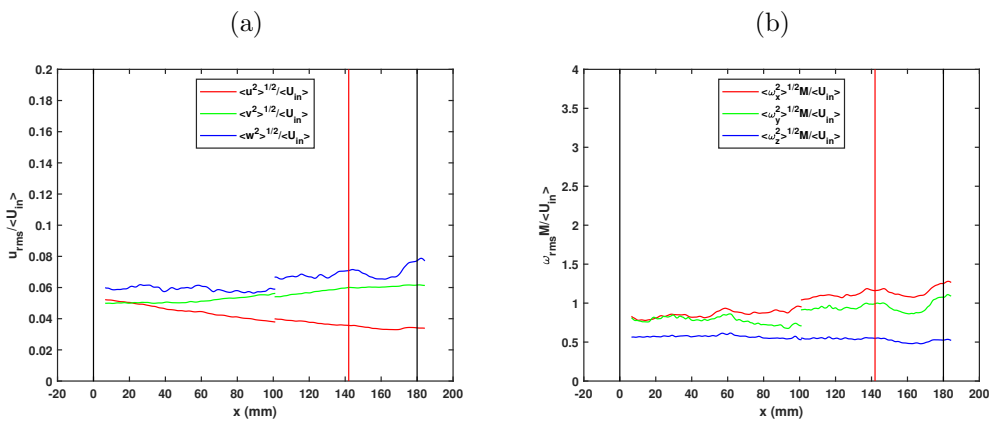

Figure S13: Streamwise evolution of (a) RMS velocity and (b) RMS vorticity for mode S1. In this case the distance between the grid and the contraction is increased using an extensional part. The black vertical lines indicate the start and end of contraction and the red line indicates the location of maximum contraction curvature.

The PDF of the alignment of coherent structures with the vertical in sub-regions R4* to R9* is shown in figure S12. The criteria for coherent structures identification were decided after a systematic analysis of cut-off values of $|\boldsymbol{\omega}|$ and volume of the structure. We choose $|\boldsymbol{\omega}|$ = 20 s^{-1} and volume of 100 voxels in this analysis. PDFs in the sub-regions also verifies the observed alignment. P2* is divided into sub-regions R4*- R6* and P3* is divided into R7*- R9*. The mid-x-locations of these sub-regions are given in the caption of figure S12. As R4* is closer to the inlet of the contraction, structures tend to have more random alignment as against other sub-regions which show preferred alignment. It is also interesting to note that the peak PDF value at the vertical orientation ($\cos(\theta_{-X-Struct})$ = 1) below the exit of contraction (R9*) is lower than that for R8*.

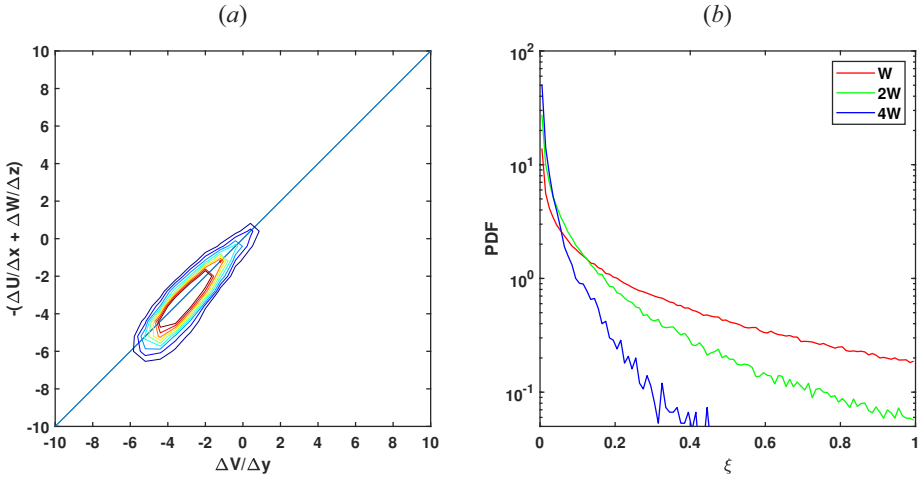

Figure S14: Continuity verification for high-magnification experiments: (a) Joint-PDF of velocity differences $\Delta V/\Delta y$ and $-(\Delta U/\Delta x + \Delta W/\Delta z)$ for a volume size of $4W$; contours are shown for the range 0.01-0.05. (b) PDF for ξ. All plots are shown for the grid of size 48 voxels.

This reversal is also seen in the previous experiments. without the extensional part in figure 21(a).

With the extensional part, we observe RMS quantities (figure S13) to vary in the same way as those seen without the extension. The local maximum at MCL followed by a decrease in w_{rms} is also seen with the extension but it is less prominent.

S7. Higher Magnification Experiments

Our experiments cannot resolve all the small scales and the velocity gradients accurately. Thus in order to evaluate the effect of spatial resolution, we repeat an experiment using a higher optical zoom ($\sim 2\times$). The measurements were made in a region 30 mm $\times$ 50 mm approximately centered about the location of the maximum contraction curvature. Higher optical zoom is achieved by moving the cameras closer to the test section. We use a smaller aperture of f/22 for sufficient depth of focus and a 5.8 mm-thick calibration plate from LaVision (Type 7). The same camera resolution of 1152 $\times$ 2016 px is used at a higher frame rate of 2000 fps. In these zoomed-in experiments, smaller 50 μm polyamid particles (PSP-50 from Dantec Dynamics) of density 1.03 g/cm^3, are used. Particle tracking is done using STB method as detailed above and the velocities are mapped to an Eulerian grid of size 48 pixels with 75% overlap with a time filter length of 5 time-steps. This gives a velocity spatial resolution of 0.32 mm compared to 0.61 mm in the lower magnification experiments used in the rest of the data.

We evaluate the quality of the experimental method by looking at the Joint-PDF of $\Delta V/\Delta y$ and $-(\Delta U/\Delta x + \Delta W/\Delta z)$, and PDF of normalized deviation from continuity, ξ as was explained in subsection 2.5. We observe the high-magnification experiments result in more accurate measurements with a higher correlation of 0.94 (from JPDF shown in figure S14(a)) for similar volume size. The mean values of ξ are 0.19, 0.1 and 0.03 for W, $2W$, and $4W$ respectively. This also indicates higher accuracy.

With higher magnification we expect more of the finer scales to be resolved and thus a comparison is made between the isotropic estimate of dissipation ε in equation 3.1 and

Parameters	Sync Mode 1	Random
	High Magnification - STB	
ε (m^2 s^{-3})	6.66×10^{-4}	6.68×10^{-4}
ε^* (m^2 s^{-3})	7.07×10^{-4}	7.36×10^{-4}
η (mm)	0.194	0.194
η^* (mm)	0.191	0.189
δ/η	1.6	1.6
	Low Magnification - STB	
ε (m^2 s^{-3})	2.44×10^{-4}	2.81×10^{-4}
η (mm)	0.249	0.241
δ/η	3.1	3.1
	High Magnification - Tomo	
ε (m^2 s^{-3})	4.82×10^{-4}	
ε^* (m^2 s^{-3})	6.31×10^{-4}	
η (mm)	0.210	
η^* (mm)	0.197	
δ/η	1.5	

Table S2: Comparison of dissipation rates and Kolmogorov scales, computed with STB, from low and high magnification experiments and the corresponding parameters calculated with the Tomo-correlation method for mode S1. The values presented are computed on the centerline of the tunnel at x =142 mm. Here δ is the velocity-grid resolution. The star superscripts indicate dissipation and the corresponding Kolmogorov scales, estimated without invoking the isotropy assumption, as is explained in the text.

an estimate using the sum of individual velocity gradients ε^*. In Table S2 we present the comparison of dissipation rates and thus Kolmogorov scales, for modes S1 and R. We also present the comparison of these values obtained from STB and the Tomo correlation methods, for mode S1. The actual definition of dissipation is $\varepsilon^* = 2\nu\langle s_{ij}s_{ij}\rangle$, where s_{ij} is the strainrate due to the fluctuating velocities. The term $\langle s_{ij}s_{ij}\rangle$ has twelve terms involving the gradients of fluctuating velocities. As the gradients of w are less accurate in the Tomographic methods, the terms involving the gradients of w are estimated in the following manner. The term $\left\langle(\partial w/\partial z)^2\right\rangle$ is taken to be the average of $\left\langle(\partial u/\partial x)^2\right\rangle$ and $\left\langle(\partial v/\partial y)^2\right\rangle$, the cross-terms $\left\langle(\partial w/\partial x)^2\right\rangle$ and $\left\langle(\partial w/\partial y)^2\right\rangle$ are taken as the average of the other four cross-terms i.e., $\left\langle(\partial u/\partial y)^2\right\rangle$, $\left\langle(\partial u/\partial z)^2\right\rangle$, $\left\langle(\partial v/\partial x)^2\right\rangle$, and $\left\langle(\partial v/\partial z)^2\right\rangle$. The values presented in the table are averaged over many realizations. In case of the high magnification experiments, they are averaged over five realizations each for both S1 and R, which are all taken on the same day. In the close-up experiments ε and ε^* compare well with a deviation of $\sim$ 10% using the above assumptions. We also notice that η computed using the estimate ε and ε^* are of similar size due to its dependence of $\varepsilon^{-1/4}$. For the correlation-based Tomo method this deviation is higher by about 30%. Due to underestimation of the dissipation rates, low magnification experiments result in only slightly larger size of η. We conclude that the isotropic approximation of ε works reasonably well in our case.

The better resolution of the velocity gradients is also manifest in larger magnitude of

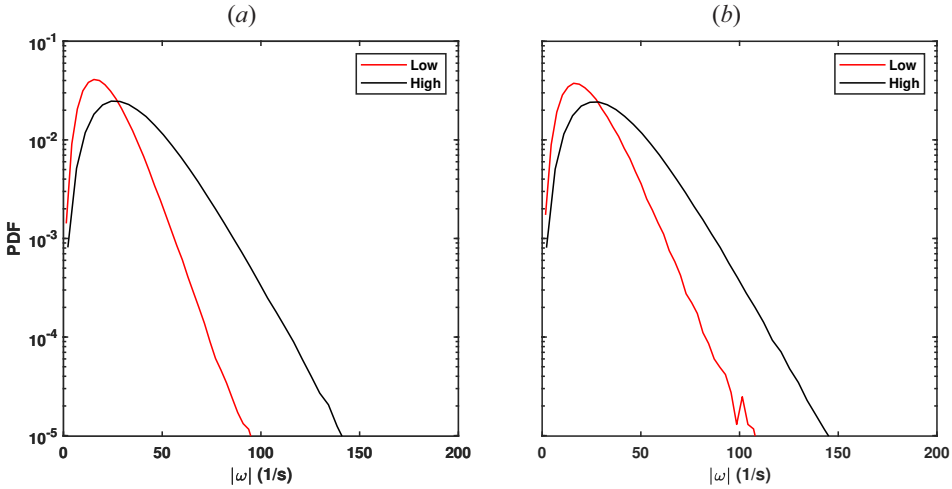

Figure S15: PDF of $|\boldsymbol{\omega}|$ obtained with low and high magnification experiments for grid oscillation modes (a) S1, and (b) R. The PDFs are obtained using data from a ~ 3 mm$\times$ 3 mm region around the tunnel centerline at x =142 mm.

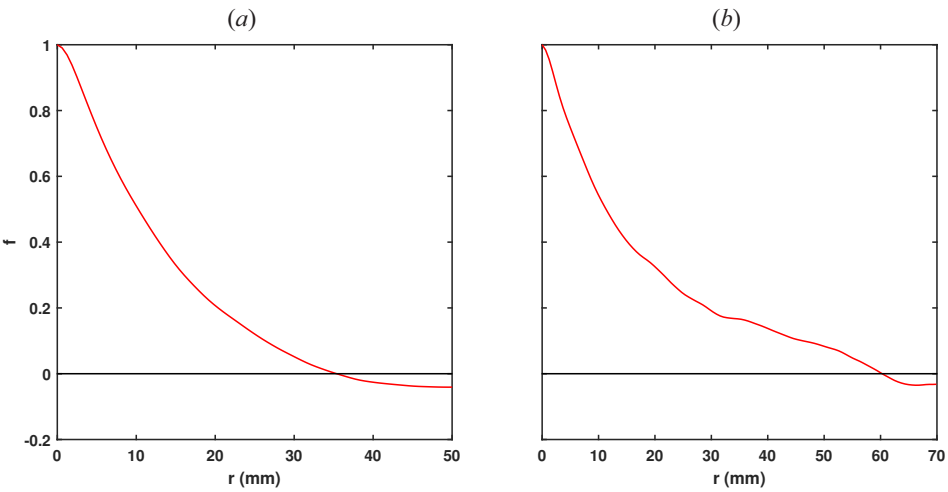

Figure S16: Streamwise correlation function $f(r_x)$ measured around $x = 30$ mm in grid-rotation modes S1 (a) and R (b).

vorticity, which is shown in the PDFs of $|\boldsymbol{\omega}|$ shown in figure S15. Similar increase was also observed previously in Casey *et al.* (2013). The PDFs for modes S1 and R have been obtained using data from a 3 mm $\times$ 3 mm region around the tunnel centerline at the maximum curvature location, $x = 142$ mm. As samples are taken from the same physical region, low magnification will have lower number of samples compared to the other case. For better convergence, PDFs are presented after averaging over five different realizations. It is clear that with higher resolution, PDF shifts to higher values of $|\boldsymbol{\omega}|$ which indicates better resolution of finer scales. However, both the resolutions will capture the same large scale structures (Casey *et al.* (2013)).